

Study of electron cloud build-up and instability in high intensity proton rings

K. Ohmi, T. Toyama, C. Ohmori
KEK, Oho, Tsukuba, 305-0801, Japan

Abstract

An e^-p instability has been observed in some proton rings. The instability, which causes beam loss, limits performance of the ring. The instability may be serious for 3 GeV and 50 GeV proton storage rings in Japan Hadron Facility (JHF). We study the e^-p instability in several high intensity proton storage rings operated in the world. This work informs JHF whether we have to take measures to cure the instability, for example apply a TiN coating on the chamber surface.

1 INTRODUCTION

The electron-proton (e^-p) instability has been discussed for a long time. The first work was done at CERN-ISR [1, 2]. An instability was observed at the operation of coasting beam and it was cured using clearing electrodes. After that, an instability has been observed for bunched proton beam in a proton synchrotron ring at Los Alamos National Laboratory (LANL-PSR) [3]. They reported that the instability was caused by an electron cloud. In their scenario, primary electrons were produced by proton losses at the chamber surface, and an electron cloud was formed by the trailing edge multi-pacting [3, 4]. Electrons, which are produced by the head part of the beam, are accelerated by the body part of beam, and released at the trailing edge. The accelerated electrons create secondary electrons at the chamber surface. The secondary electrons are amplified at every hitting of the chamber wall.

A high intensity proton accelerator facility has been proposed in Japan as a joint project of KEK and JAERI. The facility, which is named Japan Hadron Facility (JHF), is equipped by two proton rings: a 3GeV rapid cycle synchrotron and a 50GeV proton synchrotron. The bunch population, which is 4.15×10^{13} , compares with that of PSR. The electron cloud instability may be serious for these two rings of JHF.

The electron cloud instability has not been observed in all high intensity proton rings. For example, the instability has not been observed at the rapid cycle synchrotron ISIS in Rutherford Laboratory at the bunch intensity comparable with PSR. AGS has an intensity which is only a small factor different from that of JHF-50GeV, but the instability has not been observed. It is worthwhile to compare these proton rings from the point of view of the electron cloud instability. The parameters of these rings are summarized in Table 1.

The electron cloud causes both the coupled and the single bunch instabilities. A perturbation of the cloud induced by a bunch affects other bunches, and causes the coupled bunch instability. A perturbation induced by a part of a

bunch affects other part of the own bunch, and causes the single bunch instability. In these rings, bunch length and free space between bunches are several 10 m both. At a first sight, the free space of several 10m seems to be enough long to smear out perturbation of the bunch. Hence, we focus on the single bunch instability in this paper.

We discuss formation of the electron cloud in Sec.2. Electrons created by ionization and proton loss are taken into account as the primary ones. Secondary electrons are created by hitting of the original electrons on the chamber wall. The electron cloud density of each ring is estimated by a computer simulation considering the primary and the secondary electrons. We study the instability of proton beam interacting with the electron cloud in Sec.3. We analyze the instability with a tracking simulation [5] and a wake field approach [6].

2 FORMATION OF ELECTRON CLOUD

We discuss electron production and formation of the cloud. Many possibilities for primary electron production are considered. Ionization of residual gas due to proton beam creates electrons and ions. The ions create electrons when they are absorbed at the chamber surface [7, 8]. Electrons are also created by proton absorption at the beam chamber surface. H^- injection is a direct electron source. We classify the electron sources roughly into two categories for initial condition of electrons: that is, the electrons produced at the chamber surface and at the beam position.

The yield of ionization electrons is determined by the ionization cross-section and vacuum pressure in the beam chamber. Electrons are produced along the beam trajectory. Electron production at the chamber surface is rather complex. It is not well-known how many electrons are produced by proton beam, though there are many candidates. R. Macek et. al. measured number of electrons hitting the chamber wall using button electrodes at PSR [3]. They observed a peak current of $400\mu A/cm^2$ with the width of 50ns at the revolution period of 350ns with the proton current of 20A. In the positron machine, KEKB-LER, we observed electron current of $1 - 10\mu A/cm^2$ in DC at the positron current of 600mA. These measurements show that the number of electrons produced in high intensity proton rings is comparable with that of positron storage rings. It is surprising that proton rings have such a highly efficient electron production mechanism.

In KEKB, the electron current is understood to be due to photoelectron emission caused by synchrotron radiation. A probability for a positron to emit a synchrotron radiation photon at the travel distance of 1 m is 0.15, and 10% of the

Table 1: Basic parameters of the proton rings

variable	symbol	JHF				PSR	ISIS	AGS
		3GeV		50GeV				
		inj.	ext.	inj.	ext.			
circumference	$L(m)$	348.3	348.3	1567.5	1567.5	90	163	800
relativistic factor	γ	1.4	4.2	4.2	54.	1.85	1.07	3.0
bunch population	$N_p(\times 10^{13})$	4.15	4.15	4.15	4.15	3	1.25	1.2
number of bunches	n_b	2	2	8	8	1	2	6
harmonic number	H	2	2	9	9	1	2	6
rms beam sizes	$\sigma_r(cm)$	1.9	1.2	1.1	0.5	1.0	3.8	0.7
bunch length	$\ell_p(m)$	110	82	82	16	65	60	68
rms energy spread	$\sigma_E/E(\%)$	0.6	0.7	0.7	0.25	0.25		0.28
slippage factor	η	-0.48	-0.047	-0.058	-0.0013	-0.187		-0.146
synchrotron tune	Q_s	0.0058	0.0005	0.0026	0.0001	0.0003	0.0003	0.0017
beam pipe radius	$R(cm)$	12.5	12.5	6.5	6.5	5	8	5

photons create photoelectrons: i.e., the electron production rate is $Y_1 = 1.5 \times 10^{-2} e^- / (m \cdot e^+)$. The observed current value well coincides with simulations taking into account the electron yield, their motion and geometry of the button electrodes.

To explain the observed current at the proton machine, R. Macek et. al. proposed electron production due to proton loss at the chamber surface [3]. M. Furman et.al. [4] use electron production rate $Y_1 = 4.4 \times 10^{-6} e^- / (m \cdot p)$ at the chamber surface. They have observed proton loss of 4×10^{-6} per turn at PSR ($L=90m$). They assume that a proton creates 100 electrons at its loss. Though this rate is still smaller than that of KEKB, multipacting due to secondary electrons makes up the difference. The number of amplified electrons was consistent with the electron current measurement.

Since we do not have clear information about the rate for JHF, we use this primary electron yield in our calculation, although this value may depend on energy, chamber geometry, surface condition, etc.

We also investigate ionization electrons. These electrons are produced by the ionization of residual gas in the chamber. Ionization cross-section for CO and H_2 is estimated as $\sigma(CO) = 1.3 \times 10^{-22} m^{-2}$ and $\sigma(H_2) = 0.3 \times 10^{-22} m^{-2}$ using the Bethe formula [9]. The molecular density d_m is related to the partial pressure in nPa by the relation at $20^\circ C$, $d_m(m^{-3}) = 2.4 \times 10^{11} P_m(nPa)$. The electron production rate is $7.7 \times 10^{-9} e^- / (m \cdot p)$ at $2 \times 10^{-7} Pa$. The production rate is 7 orders at magnitude smaller than that of the photoelectron in KEKB, and is 3 orders smaller than that of the proton loss.

Secondary electron production plays an important role for electron cloud build-up in proton rings, because primary electrons are much less than that of positron ring. Secondary yield [10], which is the number of electrons created by an electron incidence with an energy, is approxi-

mated by the formula,

$$Y_2 = Y_s \times \frac{E}{E_{max}} \frac{1.44}{0.44 + (E/E_{max})^{1.44}}. \quad (1)$$

Fig.1 shows the secondary yield for $Y_s = 2.1$ and $E_{max} = 200eV$. These values are obtained for aluminum by measurements [11].

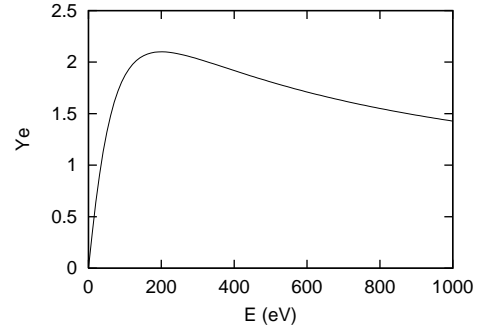


Figure 1: Secondary electron yield depending on incident electron energy for $Y_s = 2.1$ and $E_{max} = 200eV$

2.1 Simulation of electron cloud formation

Electron cloud formation is estimated by tracking the motion of electrons produced by the primary and the secondary electron emission [10, 12]. The motion of electrons is calculated in the transverse two dimensional plane. We consider electron cloud distribution at the position s_e . The distribution and line density $\lambda_e(z)$ is assumed to be dependent only on $z = s_e - vt$, but to be independent on s_e for the choice of independent variables (z, s) . We neglect space charge force between electrons in present simulation, because the average neutralization factor $\lambda_e/\bar{\lambda}_p$ is of the order of 0.1 in our case as it is seen later, where λ_e and $\bar{\lambda}_p$ are

the electron line density and the proton average line density, respectively. Therefore the results shown below are scaled by the yield of primary electrons. However electron motion during the beam passage absence is important for the survivor of electrons, which are the seeds of multipacting due to the next bunch. We will include the space charge force in the near future.

The proton beam is sliced along longitudinal direction with an equal step. Each slice has a local proton density $\lambda(z)_p$. Electrons are tracked step by step along the passage of the proton beam. Equation of motion for electrons is expressed by

$$\frac{d^2\mathbf{x}(t)}{dt^2} = -\frac{2\lambda_p(s_e - vt)r_e c^2}{(\sigma_x + \sigma_y)\sigma_y} \mathbf{F}_G(\mathbf{x}(t)), \quad (2)$$

where the force $\mathbf{F}_G(\mathbf{x})$ is expressed by the Bassetti-Erskine formula normalized so that $\mathbf{F}_G \rightarrow \mathbf{x}/|\mathbf{x}|^2$ as $\mathbf{x} \rightarrow \infty$. t is time when the beam slice at $z = s_e - vt$ arrived at electron position s_e . The equation is integrated with the time step of the slice width.

The electrons are produced at the chamber surface or at the beam position, when proton beam passes through the longitudinal positions. The number of production is proportional to the local proton density. We produce primary macro-electrons of $1.0 - 1.5 \times 10^4 e/N_p$ for a proton bunch passage in this simulation. The longitudinal charge distribution of the proton bunch is assumed to be expressed by a sinusoidal function as

$$\rho_p = \frac{\pi N_p}{2\ell_p} \sin \frac{\pi z}{\ell_p}. \quad (3)$$

The number of electrons in the chamber is calculated during passage of 10 proton bunches. Fig.2 shows the number of electrons as a function of s . The vertical axis is the number of electrons which is normalized by the number of primary electrons produced by a bunch, $A_e(z) = \lambda_e(z)/(Y_1 N_p)$. A_e characterizes the amplification factor due to secondary emission.

The electron cloud density gradually increases at the beginning of the interaction, and suddenly increases at the bunch tail. This is due to the trailing edge multipacting [4]. The number of electrons decreases after finishing of the multipacting, but considerable quantity of electrons remains in the chamber at arrival of next bunch. The quantity depends on the ring and beam parameters. Electrons accumulate gradually again with a sudden leap at the tail of the 2nd bunch. These processes, in which the number of electrons increases and decreases, are repeated every passage of bunches. The numbers of electrons at top and bottom arrive at certain values after 5-10 bunches passage. The arrived values and the number of bunches to pass depend on the ring and beam parameters.

Fig.3 shows the transverse distribution of electrons during the passage of the last (10-th) bunch. The figure shows that electrons distribute widely at the start of the interaction with the bunch and are gathered at the beam position

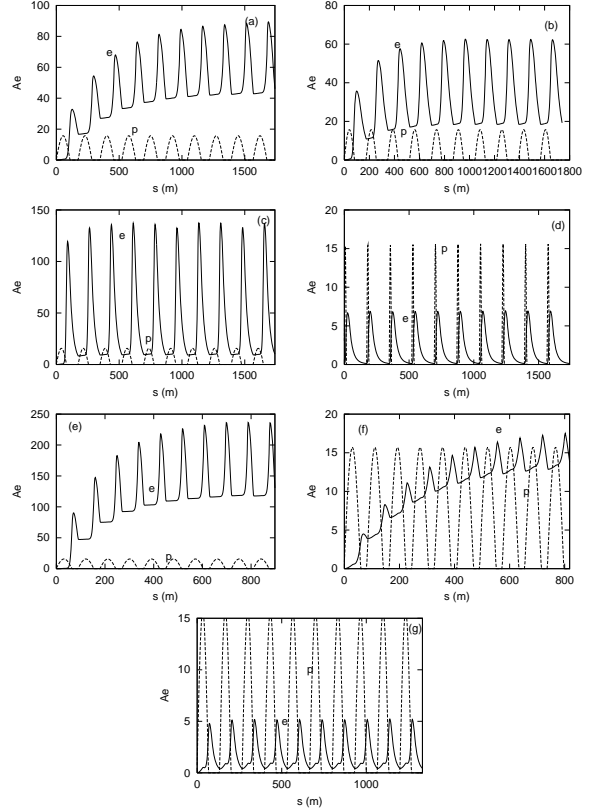


Figure 2: Electron amplification factor and proton beam density (arbit. unit). Electrons are produced at the chamber surface. (a) 3GeV inj (b) 3GeV ext (c) 50GeV inj (d) 50GeV ext. (e) PSR (f) ISIS (g) AGS

immediately, and splash after the interaction. The last picture shows the vertical distribution of electrons after 50m passage. The cloud size is comparable or a little larger than the beam size.

We also investigated electron cloud build-up due to ionization. Electrons are produced at the beam position. The initial energy of ionization electron is neglected. If the energy of electron is high enough to escape the beam potential, the production yield contributes to Y_1 at the chamber surface. Fig.4 shows the number of electrons A_e for zero initial energy. The number is far less than that produced at chamber. Electrons can not get sufficient energy to produce secondary electrons.

We now estimate neutralization factor of the electron cloud for proton beam. The proton and electron line densities are functions of z . The neutralization factor is defined as electron cloud line density divided by the average proton line density, $f(z) = \lambda_e(z)/\bar{\lambda}_p$, which is function of z . The neutralization factor is expressed by

$$f(z) = \frac{A_e(z)Y_1 N_p}{N_p/\ell_p} = A_e(z)Y_1 \ell_p. \quad (4)$$

Table 2 shows peak and bottom values of the neutralization factor for each ring. The neutralization factor strongly

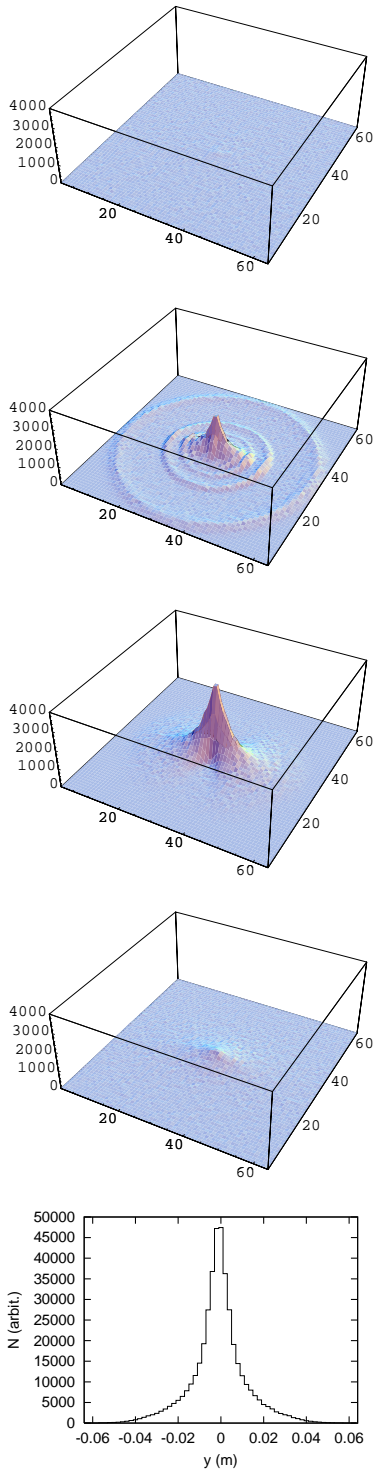


Figure 3: Transverse electron distribution during the passage of the last (10-th) bunch (1-st) 0m, (2-nd) 10m, (3-rd) 50m, and (4-th) 100m, and (5-th) vertical distribution after 50m passage.

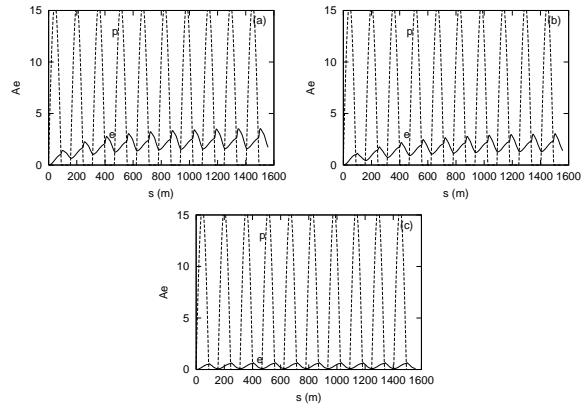


Figure 4: Electron amplification factor and proton beam density (arbit. unit). Electrons are produced at the beam position. (a) 3GeV injection (b) 3GeV extraction (c) 50GeV injection

depends on the parameters: beam size, chamber size, bunch length, and bunch spacing.

We got some characteristics concerning electron cloud in this simulation. The characteristics are used to estimate instability in the next section. They are summarized as follows,

- Electron cloud arrives at an equilibrium density after around 10 bunches passage.
- Leading-edge of the proton beam passes through the electron cloud which is formed by previous bunches. The electron cloud distributes all over the chamber.
- Electrons are gathered at the beam position immediately at the passage of the leading-edge.
- Number of electrons suddenly increases by $2 \sim 10$ times depending on the beam and ring parameters at the trailing-edge of the proton beam.

3 INSTABILITY CAUSED BY ELECTRON CLOUD

We discuss the instability caused by the electron cloud. The instability is studied by simulation using beam tracking and the wake field approach. We study the transverse dipole mode instability, in which the beam can have dipole moment $\vec{x}(z, s)$, where $\vec{x}(z, s)$ is a function of z .

3.1 Simulation using beam tracking

The electron cloud is created and accumulated by passage of bunch by bunch as is shown in the previous section. We study motion of proton bunches interacting with the electron cloud using a tracking simulation. For simplicity, we use the characteristics of the electron cloud summarized in the previous section. Electrons are assumed to be always uniformly distributed with a certain density in

Table 2: Electron cloud build-up of the proton rings

variable	JHF				PSR	ISIS	AGS
	3GeV		50GeV				
	inj.	ext.	inj.	ext.			
$A_e(\text{bottom})$	42.0	18.0	9.4	0.13	118.	12.9	0.42
$A_e(\text{peak})$	87.6	62.	136.	6.9	236.	17.5	5.18
$\eta(\text{bottom})$	0.020	0.0067	0.0035	0.00001	0.034	0.003	0.0001
$\eta(\text{peak})$	0.042	0.023	0.05	0.0005	0.067	0.005	0.0015

the vacuum chamber at the beginning of interaction with a proton bunch: that is, they do not have memory due to interactions with previous bunches.

A proton bunch is represented by macro-particles which are located along z with equal spacing. Each macro-particle has a charge and a mass corresponding to the proton line density. The macro-particle is free for dipole motion with dipole moment characterized by $\bar{x}_p(z_i, s) = (\bar{x}_p, \bar{y}_p)$, but the emittance (size) is kept to be constant. Electron cloud is set at one or some positions of the ring, and is represented by a large number of point-like macro-particles. The electrons are initialized by uniform distribution in every interaction with the beam.

The equation of motion is expressed by

$$\frac{d^2 \bar{x}_{p,i}}{ds^2} + K(s) \bar{x}_{p,i} = -\frac{2r_p}{\gamma} \sum_{a=1}^{N_e} \mathbf{F}_G(\bar{x}_{p,i} - \mathbf{x}_{e,a}; \boldsymbol{\sigma}) \quad (5)$$

$$\frac{d^2 \mathbf{x}_{e,a}}{dt^2} = -2\lambda_p(z) r_e c \mathbf{F}_G(\mathbf{x}_{e,a} - \bar{\mathbf{x}}_{p,i}; \boldsymbol{\sigma}). \quad (6)$$

Motion of the macro-electrons and macro-protons is tracked during the beam passage. After that, macro-protons are transferred by the lattice magnets, and then interact with randomly initialized electrons again. These procedures are repeated in every interaction of the bunch and cloud.

We performed the simulation for JHF 3GeV and 50GeV rings at injection. The neutralization factor was 2% and 4% for 3GeV and 50GeV rings, respectively. These value are bottom values in the Table 2. Fig.5 shows the vertical dipole moment of a proton bunch $y_p(z_i, s)$ along the longitudinal position z at $s = 20 \times L$. Excitation of dipole mode with the frequency ω_e is seen. We got similar signal for the horizontal moment.

Fig.6 shows the variation of dipole moment, J_y , where $J_y = (\gamma y^2 + 2\alpha y y' + \beta y'^2)/2$ is maximum value along z .

To discuss the beam stability, we compare the growth rate with the Landau damping rate. We take into account the Landau damping caused by longitudinal motion of bunch, which disturbs the coherence of the dipole motion. Landau damping rate is given by $\omega_e \eta \sigma_\delta = \omega_s \omega_e \sigma_z / c$ for a long bunched beam [13]. The beam stability is estimated by these ratios,

$$U \equiv \frac{\sqrt{3}}{\Delta \omega \tau_g} = \frac{\sqrt{3} T_0 / \tau_g}{2\pi \nu_s \omega_e \sigma_z / c}. \quad (7)$$

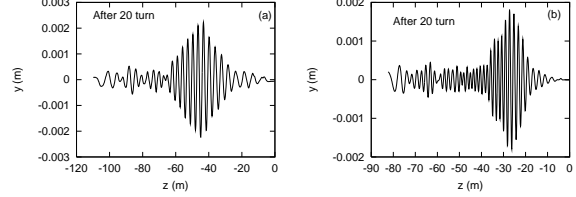


Figure 5: Vertical dipole moments for JHF 3GeV and 50 GeV rings at injection. The right-left correspond to the head-tail of a bunch, respectively. Pictures (a) and (b) are obtained for 3 GeV and 50 GeV, respectively.

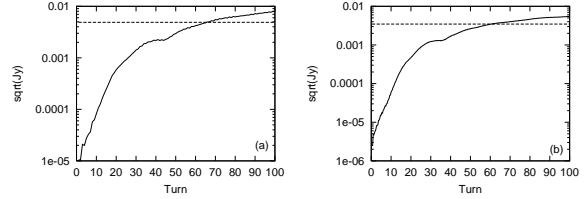


Figure 6: Growth of the vertical dipole instability for JHF 3GeV and 50 GeV rings at injection. The right-left correspond to the head-tail of a bunch, respectively. Pictures (a) and (b) are obtained for 3 GeV and 50 GeV, respectively.

where $\sqrt{3}$ is used as a normal stability condition.

For JHF 3GeV and 50 GeV at injection, the growth rate T_0/τ_g for small amplitude is $0.2 (< 0.1\sigma_r) \sim 0.1 (\approx 0.1\sigma_r)$ in the both cases. U is obtained as

$$U = 0.15 \sim 0.07 \quad 3\text{GeV} \quad (8)$$

$$U = 0.23 \sim 0.12 \quad 50\text{GeV}. \quad (9)$$

Although the growths in Figure 6 are very fast, Landau damping suppresses the instability because of large $\omega_e \sigma_z / c$.

3.2 Wake field induced by electron cloud and beam stability

Here we treat the instability with analytic approach using the wake field induced by electron cloud. We know that the electron cloud was gathered near to the beam immediately at beginning of the interaction with the beam, and the beam

interacted with the pinched electron distribution during the passage through the cloud. The size of electron cloud is about the same as the beam size. We regard the system as an interaction between the coasting beam and the electron cloud with Gaussian distribution. We take linear term of the interaction. The motions of the beam and electron cloud are characterized by $y_p(s, z)$ and $y_e(s, t)$, respectively. The equations of motion for the beam and cloud are expressed as follows,

$$\begin{aligned} \frac{d^2 y_p(s, z)}{ds^2} + \left(\frac{\omega_{\beta, y}}{c}\right)^2 y_p(s, z) \\ = - \left(\frac{\omega_{p, y}}{c}\right)^2 (y_p(s, z) - y_e(s, (s+z)/c)) \end{aligned} \quad (10)$$

$$\frac{d^2 y_e(s, t)}{dt^2} = -\omega_{e, y}^2 (y_e(s, t) - y_p(s, ct - s)), \quad (11)$$

where $\omega_{\beta, y}$ denotes the angular betatron frequency without electron interaction. The two coefficients $\omega_{p, y}$ and $\omega_{e, y}$ characterize the linearized force between the beam and cloud, and are given by

$$\omega_{p, y}^2 = \frac{\lambda_e r_e c^2}{\gamma(\sigma_x + \sigma_y)\sigma_y}, \quad \omega_{e, y}^2 = \frac{\lambda_p r_e c^2}{(\sigma_x + \sigma_y)\sigma_y}, \quad (12)$$

where λ_e and λ_p are the line densities of the cloud and beam, and σ_x and σ_y are the horizontal and vertical beam sizes, respectively.

From Eq.(10) and (11), an equation for the beam motion is obtained as follows,

$$\begin{aligned} \frac{d^2 y_p(s, z)}{ds^2} + \left(\frac{\tilde{\omega}_{\beta}}{c}\right)^2 y_p(s, z) \\ = \frac{\omega_p^2 \omega_e}{c^3} \int_z^\infty y_p(s, z') \sin \frac{\omega_e}{c} (z - z') dz'. \end{aligned} \quad (13)$$

Here $\tilde{\omega}_{\beta}^2 = \omega_{\beta}^2 + \omega_p^2$ is the angular betatron frequency including the frequency shift due to the electron cloud. The right-hand side of Eq.(13) can be represented by a wake function, which depends only on the longitudinal distance. Integrated over the ring circumference L , the wake function can be written as

$$W_1(z)[m^{-2}] = cR_S/Q \sin\left(\frac{\omega_e}{c}z\right), \quad (14)$$

where

$$cR_S/Q = \frac{\lambda_e}{\lambda_p} \frac{L}{(\sigma_x + \sigma_y)\sigma_y} \frac{\omega_e}{c}. \quad (15)$$

This wake field does not damp for z in this model: i.e., in the word of impedance, the Q factor is infinite. Actually the frequency spread of ω_e should be taken into account. We add a damping term $2\alpha y_e$ in the left hand side of Eq.(11). The damping factor α corresponds to the frequency spread of ω_e . The wake field is now expressed by

$$W(z) = c \frac{R_S}{Q} \frac{\omega_e}{\tilde{\omega}} \exp\left(\frac{\alpha}{c}z\right) \sin\left(\frac{\tilde{\omega}}{c}z\right), \quad (16)$$

where $\alpha = \omega_e/2Q$ and $\tilde{\omega} = \sqrt{\omega_e^2 - \alpha^2}$. Note that $z < 0$ for backward direction.

In this framework the frequency spread (α or Q) is not determined. The spread is caused by nonlinear interaction with beam, proton distribution along z and beam size modulation due to β function variation. An estimation of Q caused by nonlinear interaction is given in Ref.[6]. The wake field is calculated by the same simulation method. Fig.5 shows the wake field for JHF-50GeV at injection. The resonator parameters are obtained by fitting the figure

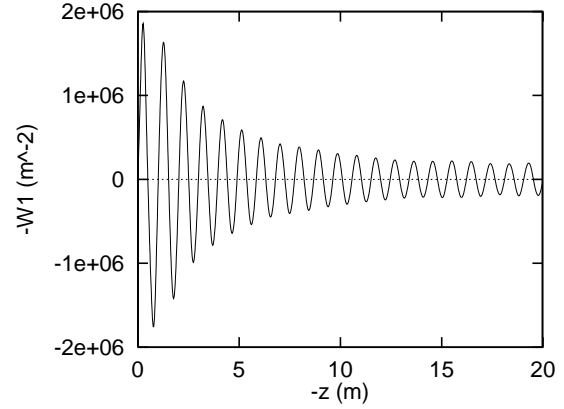


Figure 7: Wake field caused by electron cloud for JHF 50 GeV at injection.

as follows,

$$\begin{aligned} \frac{cR_S}{Q} &= 1.9 \times 10^6 m^{-2} \quad (1.1 \times 10^6 m^{-2}) \\ \omega_e &= 1.9 \times 10^9 s^{-1} \quad (1.2 \times 10^9 s^{-1}) \\ Q &= 13. \end{aligned} \quad (17)$$

The number enclosed in brackets is analytical value given by Eqs.(12) and (15). cR_S/Q and ω_e are somewhat larger values than the analytical ones. $Q=13$ was obtained by the simulation with the account of the nonlinearity of the beam-cloud interaction. The Q value is conjectured to be further reduced for considering the longitudinal proton distribution and modulation of the beta function.

Corresponding effective transverse impedance is given by Fourier transformation of the wake field.

$$\begin{aligned} Z_1(\omega) &= \frac{c}{\omega} \frac{R_S}{1 + iQ \left(\frac{\omega_e}{\omega} - \frac{\omega}{\omega_e}\right)} \\ &= \frac{\lambda_e}{\lambda_p} \frac{L}{\sigma_y(\sigma_x + \sigma_y)} \frac{\omega_e}{\omega} \frac{Z_0}{4\pi} \frac{i}{\left(\frac{\omega}{\omega_e} - \frac{\omega_e}{\omega}\right) + i\frac{1}{Q}}, \end{aligned} \quad (18)$$

where Z_0 is the vacuum impedance 377Ω .

We discuss the stability of beam which experiences the effective impedance. Since the bunch length is very long, $\omega_e \ell/c \gg 1$, the coasting beam approximation is used. The

stability criterion is given by the dispersion relation as follows [13],

$$U \equiv \frac{\sqrt{3}\lambda_p r_0 \beta \omega_0}{\gamma \omega_e \eta \sigma_\delta} \frac{|Z_\perp(\omega_e)|}{Z_0} = \frac{\sqrt{3}\lambda_p r_0 \beta}{\gamma \nu_s \omega_e \sigma_z / c} \frac{|Z_\perp(\omega_e)|}{Z_0} = 1. \quad (19)$$

For $U > 1$, the beam is unstable. U for various rings are calculated using Eq.(15) and parameters in Table 1 and 2. The Q value is 5. The results on the stability are shown in Table 3.

The table includes two values of U_H and U_L , which are the criteria for the peak and bottom values of neutralization factor, respectively. It is the same meaning for $Z_{H(L)}$.

This result, which shows that the e^-p instability is serious for PSR but is not for ISIS, is consistent with experimental results. In JHF, some of U_H exceed 1.

4 CONCLUSION

We discussed the electron cloud build-up and instability in some high intensity proton rings shown in Table 1. We studied the electron cloud build-up using a computer simulation. Primary electrons were produced at the chamber surface or at the beam position. We considered the yields of $Y_{1,\ell} = 4.4 \times 10^{-6} / (m \cdot p)$ at the chamber surface. The electrons appear due to proton loss, ion hitting or other mechanisms. The ionization yield was $Y_{1,i} = 7.7 \times 10^{-9} / (m \cdot p)$ (2×10^{-7} Pa). The ionization electron can be neglected for the vacuum pressure less than 10^{-5} Pa, if we use the yield $Y_{1,\ell}$ from the chamber surface.

The primary electrons are amplified by the secondary electron emission at the chamber surface. The electrons experience the energy gain due to the beam force, create secondary electrons, and cause multipacting. The amplification rate was estimated to be an order of 100 in the present model. The neutralization factors for some proton rings are summarized in Table 2. We have to note that the rate depends on the secondary yield, beam shape and chamber geometry. It has to be kept in mind that Y_1 is difficult to estimate in individual machines.

In this calculation, the space charge force between electrons and the elastic scattering (reflection) of electrons [14] are not considered. These may be important, because elastic scattering continues to supply electrons up to the space charge limit. We should not discard the ionization as the electron source [15].

The beam stability is estimated by a tracking simulation and coasting beam model using the wake field due to the electron cloud. The results are summarized in Table 3. The tracking simulation showed consistent results as the coasting beam model. In the results, PSR was the most severe for the instability, while ISIS was safe. JHF-3GeV is medium between PSR and ISIS. For large scale rings, AGS is safe. JHF-50GeV is more severe than AGS. Since the stability criterion U exceeds 1 at the peak cloud density for 50GeV ring, and is closed to 1 for 3GeV ring, we have to take care of the instability. We should estimate the cloud density more carefully, including the space charge between

electrons, elastic scattering of electrons, effects of lattice magnet, etc.

The secondary electrons play important roles for the electron cloud instability in proton rings. Application of the TiN coating to reduce the secondary yield is a very powerful cure for this instability.

The authors thank A. Valishev for reading this manuscript.

5 REFERENCES

- [1] H.G. Hereward, CERN 71-15 (1971).
- [2] E. Keil and B. Zotter, CERN-ISR-TH/71-58 (1971).
- [3] R. J.Macek, et. al., Proceedings of Part. Accel. Conf. 2001, 688 (2001)
- [4] M. A.Furman, M. Pivi, Proceedings of Part. Accel. Conf. 2001, 707 (2001)
- [5] K. Ohmi and F. Zimmermann, Phys. Rev. Lett., **85**, 3821 (2000).
- [6] K. Ohmi, F. Zimmermann, E.Perevedentsev, Phys. Rev. E **65**, 16502 (2002).
- [7] R. J.Macek, private communications.
- [8] Y. Mori, private communications.
- [9] Y. Baconnier, CERN report 85-19, pp.267 (1985).
- [10] M. A.Furman and G. R.Lambertson, Proceedings of MBI97, KEK Proceedings 97-17, 170 (1997).
- [11] T. Toyama et.al., in this proceeding,
- [12] K. Ohmi, Phys. Rev. Lett., **75**, 1526 (1995).
- [13] A.W. Chao, *Physics of Collective Beam Instabilities in High Energy Accelerators*, Wiley-Interscience Publication.
- [14] V. Baglin et. al., LHC-Project-Report-472.
- [15] F. Zimmermann, Proceedings of Chamonix XI, CERN-SL-2001-003 DI.

Table 3: Wake field and stability for electron cloud instability

variable	JHF				PSR	ISIS	AGS
	3GeV		50GeV				
	inj.	ext.	inj.	ext.			
$Z(\omega_e)_L/Q (M\Omega/m)$	0.29	0.24	0.68	0.019	0.46	0.0051	0.024
$Z(\omega_e)_H/Q (M\Omega/m)$	0.61	0.83	9.7	0.96	0.90	0.0085	0.37
$\omega_e \ell_p/c$	133	182	199	276	166	27	153
U_L	0.07	0.23	0.11	0.02	1.6	0.09	0.004
U_H	0.15	0.78	1.6	1.2	3.2	0.14	0.06